Rock and Soil Mechanics

Volume 43 | Issue 9 Article 4

10-31-2022

Experimental study of fracture dynamic evolution process of grouted specimen under uniaxial compression based on CT scanning

Chang-xing ZHU

Jia-xin SUN
823821653@qq.com

Yan-wei WANG

Custom Citation

ZHU Chang-xing, SUN Jia-xin, WANG Yan-wei. Experimental study of fracture dynamic evolution process of grouted specimen under uniaxial compression based on CT scanning[J]. Rock and Soil Mechanics, 2022, 43(9): 2493-2503.

Rock and Soil Mechanics 2022 43(9): 2493−2503 ISSN 1000−7598
https: //doi.org/10.16285/j.rsm.2022.5407 rocksoilmech.researchcommons.org/journal

Experimental study of fracture dynamic evolution process of grouted specimen under uniaxial compression based on CT scanning

ZHU Chang-xing, SUN Jia-xin, WANG Yan-wei
School of Engineering, Henan Polytechnic University, Jiaozuo, Henan 454000, China

Abstract: To study the fracture dynamic evolution process of grouted specimens under loading conditions, the graded gravel grouted specimen was periodically scanned during the uniaxial compression damage process using a CT scanning system. Based on the image reconstruction technique, the spatial visualization of the fracture structure inside the test grouted specimen block is achieved, and the structural characteristic parameters are characterized quantitatively such as the number and volume of fractures. The gray value and fractal dimension of the CT slices are calculated using Python programming to analyze the mesoscale damage extent at different loading stages of the grouted specimen. It is shown that the specimen's internal fracture volume shows a trend of slow rise, slow fall, slow rise, and rapid rise. The fracture number shows a trend of increasing firstly and then decreasing during the whole compression stage. When the fracture propagation paths encounter gravel, most of the fractures propagate around the gravel location and few fractures propagate through the gravel. In addition, the fracture bifurcation propagation mostly appears at the interface between the cement matrix and gravel. The specimen damage process could be divided into four stages in terms of the fracture evolution process inside the specimen: initial defect propagation stage, internal crack compacting stage, fracture propagation stage, and fracture penetration stage. For the slice at the same loading stage of the test specimen, it is found that the value of the damage variable and fractal dimension shows a certain positive correlation, which is similar to the trends of the fracture volume evolution. The research results can provide a reference for the study of the failure process and fracture evolution law of the grouted body.

Keywords: CT scan; grouted body; digital reconstruction; fracture evolution; quantitative characterization

1 Introduction

The issue of rock and soil mass stability has become more complex in underground engineering construction projects as the rapid development of urban underground space[1−2]. The sand layer is a common unfavorable geology body with poor self-stability and great hazard, which can lead to disasters such as sand collapse, cave-in, and surface collapse[3]. Grouting reinforcement technology has been widely used in sand layer treatment due to the low cost and the capability of enhancing the overall mechanical and permeation resistance properties of the sand layer[4]. During the process of grouting reinforcement, the strength characteristics of the slurry consolidation body are especially important to the reinforcement effect, while ordinary cement grouting has many defects. Many studies have been conducted on the topic of grouting reinforcement materials. Polymers such as vinyl acetate-ethylene copolymer emulsions can reduce the porosity of the cement matrix and make the pore gradation more reasonable due to the characteristics of softness and excellent deformation coordination properties[5−6]. Ultrafine cement can improve the situation that conventional cement particles are difficult to inject into fractures with a radius of 0.2 mm, reduce the thickness of the interface transition zone and improve the macroscopic cohesion of the grouted body[4, 7].

In recent years, scholars have conducted many laboratory tests on the strength, deformation behavior, and fracture evolution law of prefabricated defective grouted specimens. Wang et al.[8] used DBP toughened epoxy resin slurry to grout rock-like specimens with prefabricated fractures, the strain field of the fracture tip and the damage mechanism of multi-fracture specimens were investigated before and after grouting. For the grouting-reinforced red sandstone body, Wang et al.[9] and Wang et al.[10] investigated the fracture propagation and damage morphology of the specimen under UCS tests and established a damage evolution model. Wang et al.[11] studied the effect of different water-cement ratios on the mechanical properties and fracture features of the grouting-reinforced fractured surrounding rock bodies with different grain sizes. Le et al.[12] and Lu et al.[13] conducted mechanical properties tests on grouted specimens with inner defects, and they found that the overall strength of the specimen was significantly affected by the location and number of defects, and the damage occurred firstly at the defect location.

Received: 31 March 2022 Revised: 27 May 2022
This work was supported by the National Natural Science Foundation of China (51874119), the Department of Education Project of Henan Province (2011A440003) and the Doctorate Fund of Henan Polytechnic University (B2009-96).
First author: ZHU Chang-xing, male, born in 1976, PhD, Associate Professor, mainly engaged in research on soft rock deformation and its control. E-mail: zcx@hpu.edu.cn
Corresponding author: SUN Jia-xin, male, born in 1998, Master student, majoring in grouting reinforcement of rock and soil mass. E-mail: 823821653@qq.com

Grouting-reinforced body is a widely used composite multi-scale material[14−15]. Most of the previous studies on the grouting-reinforced body have been conducted at the macroscopic scale, while the macroscopic fracture damage and destabilization of the grouting-reinforced body under external loading are closely related to the internal microporosity distribution and the initiation, propagation, and coalescence of micro fractures[16−17]. By using the CT technique, Yang et al.[18] studied the fracture development and the fractal dimension evolution of the grouted specimens. Bharath et al.[19] observed the grouting effect of cement−asphalt slurry using the CT technique, and they analyzed the fracture volume percentage and connectivity in the grouting-reinforced body. Zhu et al.[20] and Fan et al.[21] obtained the mesoscale damage evolution of concrete specimens based on CT test images, and characterize quantitatively the damage process of specimens using CT. Sun et al.[22] carried out uniaxial compressive strength(UCS) tests on precast defective concrete, analyzed the effect of initial defects on the fracture development, and revealed the mechanism of the fracture propagation using CT scan images.

To study the evolution process of mesoscopic pore structure of the grouting-reinforced body under UCS, the mesoscale damage characteristics have to be investigated for the grouted specimens. Considering a large number of micro fractures that exist in the sand layer, the graded gravel is selected as the material to be injected and the grouted specimen is then scanned during the UCS using a CT scanning system. The mesoscopic pore structure evolution law is described for the grouting-reinforced body. The structural characteristic parameters are characterized quantitatively such as the number and volume of fractures within the specimens using image processing. The damage variables and fractal dimensions of different slices are then calculated at different loading stages of the grouted specimen. The damage process, mechanical properties, and fracture propagation behavior are explored for the grouting-reinforced body. The research results can provide a reference for the study of the failure process and fracture evolution law of the grouting-reinforced body.

2 Test materials and methods

2.1 Preparation of grouted specimens

In this study, the indoor grouted specimens are used hereafter, which mainly consist of grouting material and graded gravel. The cement paste is used as grouting material, and the ground mixing ratio is determined through indoor orthogonal tests and other factors such as the grout injectability and the grouting effect[23−24], as shown in Table 1.

Table 1 Grout mixing ratio

Material	m_C /kg	m_W /kg	m_{VAE} /kg	m_A /kg
Grout	803.10	642.48	40.16	4.02

Note: m_C, m_W, m_{VAE}, m_A are the mass of cement, water, VAE emulsion (vinyl acetate-ethylene copolymer emulsion) and defoamer in 1 m^3 of grout, respectively.

To simulate the working scenario of massive micro-fractures that exist in the sand layer, graded gravel with controllable particle size is therefore selected as the grouting material. To minimize the porosity of the grouting material and achieve the most compact accumulation state[25], the gravel grading is calculated according to the Fuller grading curve:

$$P = 100\left(\frac{D_s}{D_m}\right)^h \quad (1)$$

where P is the total amount of material smaller than the particle size D_s; D_s and D_m are the sieve size and the maximum particle size, respectively.

The range selection of h is 1/3−1/2. When h = 1/2, the graded gravel reaches the maximum density theoretically, and the value of h is therefore 1/2 in this test. The particle size ranges from 0.15 to 4.75 mm, and Table 2 gives the calculation results from Fuller's gradation formula.

Table 2 Calculation results of the Fuller curve

Square sieve size /mm	4.75	2.36	1.18	0.60	0.30	0.15
Percent passing P /%	100.00	70.49	49.84	35.54	25.13	17.77

The results in Table 2 are arranged to obtain the ideal gradation of the grouting material based on the calculation results from Fuller's gradation equation, and the detailed parameters are shown in Table 3. The dosage per liter of different gravel sizes is calculated based on the dry density of gravel (1.49 g /cm^3) and the percent retained calculated by the Fuller curve. Fig.1 shows the gravel grading curve.

Table 3 Gravel gradation

Gravel sizes /mm	Percent retained(PR) /%	Cumulative percent retained(CPR) /%	Dosage per liter /kg
⩾4.75	0.00	0.00	0.000
[2.36, 4.75)	35.87	35.87	0.534
[1.18, 2.36)	25.10	60.97	0.373
[0.60, 1.18)	17.42	78.39	0.259
[0.30, 0.60)	12.66	91.05	0.189
[0.15, 0.30)	8.95	100.00	0.133
<0.15	0.00	0.00	0.000

The grouted specimens are obtained from indoor grouting tests, and the grouting mold size is Φ330 mm× 220 mm, as seen in Fig.2. When the grout is solidified and the mold is then dismantled after the grouting process, the test specimens are cored and polished based on the size of the standard cylindrical specimens (Φ50 mm× 100 mm). The specimens are then placed in a curing box

and cured to the given age, as shown in Fig.3.

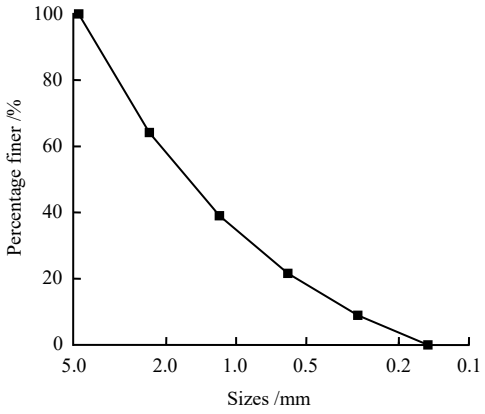

Fig. 1 Gravel grading curve

Fig. 2 Grouting model

Fig. 3 Standard test specimens of grouting-reinforced body

2.2 Test method

The test equipment is the loaded coal rock industrial CT scanning system (Phoenix v|tome|x S model), which was selected from General Electric Co., Ltd., as seen in Fig.4(a). According to the different absorption coefficients of X-rays for different components and densities within the object, the CT scanning system can reconstruct the internal structure information of the scanned object using multi-angle transmission images, information digitization, and algorithms. Fig.4(b) shows the schematic diagram of the industrial CT scanning system.

The uniaxial in-situ loading test is conducted on standard cylindrical specimens (Φ50 mm×100 mm) using an industrial CT system, and the fracture evolution process of the grouted specimens is observed under different compression loading levels. The uniaxial compression tests are conducted on three standard cylindrical grouted specimens with the same batch, specification and curing age(28 d), the average peak load strength is then obtained. By combining with the full stress-strain curve under uniaxial compressive loading, five CT scans are performed at different loading levels during the whole compression damage process for the same grouted specimens, the five loading levels are designed following the order of 0%, 20%, 40%, 90% of the peak load average value and the load σ_F of the damaged specimens, as shown in Fig.5. σ_{max} is the peak strength of the specimen.

(a) CT scanning system (Phoenix v|tome|x S model)

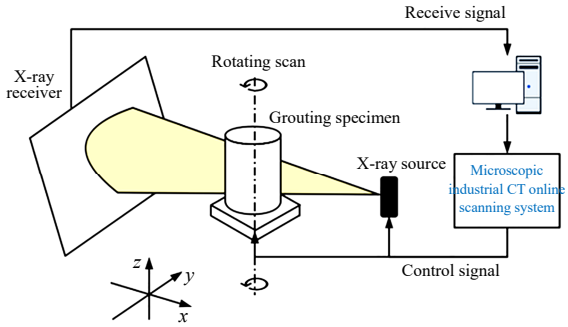

(b) The industrial CT schematic diagram

Fig. 4 Industrial CT scanning system

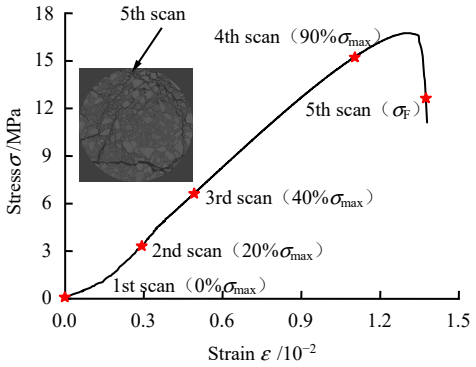

Fig. 5 Schematic diagram of CT scanning loading of grouting-reinforced body

For the grouted test specimen, a high-power micron-

focus ray source with a detail resolution ≤2 μm is selected for scanning, and 1 000 images are acquired for each scan with an exposure time of 1 000 ms. The image resolution is 55 μm. Before the specimen is loaded, a pre-pushing force is applied in advance to ensure that the end face of the specimen is completely in close contact with the bearing plate, and the grouted specimen is then loaded at a rate of 0.1 mm /min until reaching the designed load level. Using micrometer tubes, in-situ full section nondestructive scanning is performed for the grouted specimen, and the loading continues to the next loading level after scanning is completed, and so on until the 5th scan is completed. The reconstruction area is selected by phoenix datos|x2 software based on the CT scan results, and the optimal image processing effect is achieved by logarithmic filtering, geometry and beam hardening correction operations. The VG Studio MAX image processing software is then used to reconstruct slices to obtain the internal fracture distribution and structural characteristic parameters of the grouted specimen.

3 Test results and analysis

3.1 2D fracture propagation analysis

Before the analysis of fracture evolution, the different material properties are defined differently in CT slices, and the grouted specimens are simplified into three phases: large-size gravel, cement-based materials (mixture of cement, sand, etc.), and fractures. From the principle of CT scanning, it is known that the brighter color in the image indicates a greater gray value and a greater density of material properties, therefore, the gray-white part of the slice image represents large-size gravel, the gray-black part means the cement-based material, and the black part stands for the fractures, as shown in Fig.6.

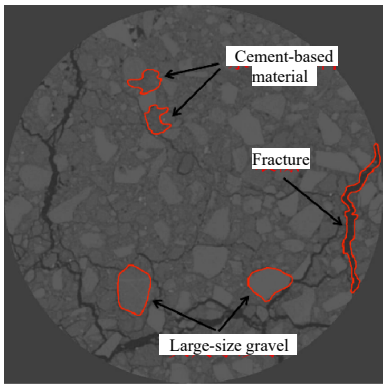

Fig. 6 Material properties of slice

Real-time information on each cross-section can be obtained using the CT scan for the grouted specimen. The fractures on the acquired cross-sectional slices are extracted and characterized using VG Studio MAX software, and the fractures are highlighted with different colors depending on the extension extent. To visually characterize the internal structure and fracture evolution process of the loaded specimen, the 200th, 500th, and 700th layers from the bottom to the top are selected from the 1 000 images of each scan as the representatives for analysis, as shown in Fig.7. Fig.8(a) and Fig.8(b) show the binary processing of slice images using MATLAB. The pixel points that correspond to fractures are extracted, and based on the pixel point proportion to the overall pixel points in the image, the fracture area on the slice is calculated. Fig.8(c) shows the fracture area variation pattern of the slice.

It is seen from Figs.7 and 8 that for the 1st scan, many original small volume point defects are observed within the specimen, and they are distributed randomly and mostly located along the boundaries of the large size gravels. For the 2nd scan, the blue area increases slightly (i.e., area a, b). For instance, the fracture area increases from 5.75 mm^2 to 7.75 mm^2 and from 17.25 mm^2 to 42.5 mm^2 for the 200th-layer and 700th-layer slices, respectively. In the meantime, some small volume fractures are closed, and the increasing extent of the blue area is greater than the decreasing extent, which shows an overall increasing trend for fracture area. For the 3rd scan, some blue areas disappear and the fracture area tends to decrease as a whole (such as area c). For instance, the fracture area decreases from 9.75 mm^2 to 8.75 mm^2 at the 500th-layer section. When the axial load is smaller than 40% of the peak load, no macroscopic fractures are generated inside the specimen. While for the 4th scan, due to the continuous action of axial loading, the original point defects further propagate inside the specimen. The fractures are connected in some certain area (such as Fractures A and B), and the fracture area increases remarkably. In addition, for the 5th scan, the peak stress reaches the UCS value of the specimen and enters into the residual stress state. Fractures A and B develop rapidly and coalesce to form dominant fracture. The fracture width increases rapidly and the fracture is fully developed. The secondary Fractures C and D in the middle of the specimen slice increase significantly in both their area and length. The internal fractures continue to interact and converge until a complex fracture network is formed, and the specimen is finally damaged.

Based on the comparative analysis of the three image groups, it is found that the main fracture normally propagates along the boundaries when the specimen fails. This is due to the fact that under the axial loading condition, the internal part of the block is in a multi-axial complex stress state, while the external part is in a bi-axial stress state, resulting in tensile failure to occur along its boundaries. A large

number of derivative fractures are developed around the main fracture during the evolution process, and a small number of secondary fractures are generated in other areas. When the fracture propagation paths encounter gravel, most of the fractures develop around the gravel boundaries, as shown in Figs.9(a) and 9(b). Additionally, very few fractures propagate through the gravel block, as seen in Figs.9(c) and 9(d), and the fracture bifurcation propagation mostly appears at the interface between the cement matrix and gravel.

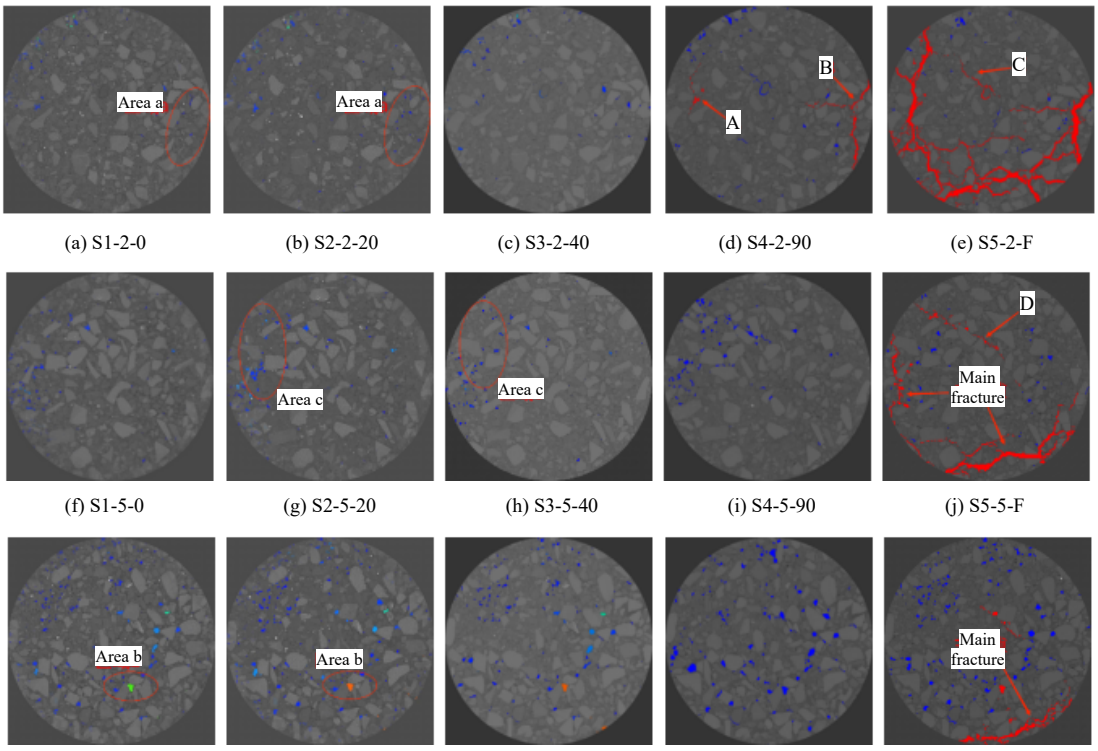

(a) S1-2-0 (b) S2-2-20 (c) S3-2-40 (d) S4-2-90 (e) S5-2-F

(f) S1-5-0 (g) S2-5-20 (h) S3-5-40 (i) S4-5-90 (j) S5-5-F

(k) S1-7-0 (l) S2-7-20 (m) S3-7-40 (n) S4-7-90 (o) S5-7-F

Note: the code rule in Fig. 7 is: scan times-first digit of the slices layer number-load level, e.g. S1-2-0 indicates that the 1st scan image of the 200th-layer slice, the load level is 0% of the peak load, and the load level F indicates the damaged specimen. In the slice image, individual fracture area $S<5$ mm^2 is indicated in blue, the area of 5 mm$^2\leqslant S<10$ mm^2 is indicated in green, and the area of $S\geqslant 10$ mm^2 is indicated in orange-red.

Fig. 7 2D fracture slice diagram of grouted specimen

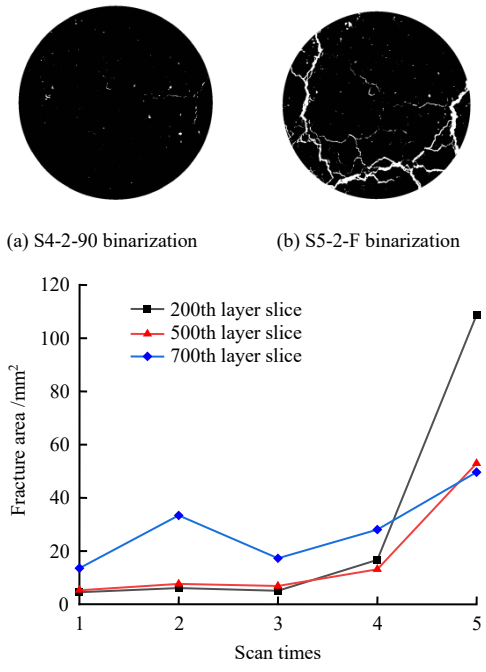

(a) S4-2-90 binarization (b) S5-2-F binarization

(c) Variation pattern of slice fracture area

Fig. 8 Slice binarization and fracture area

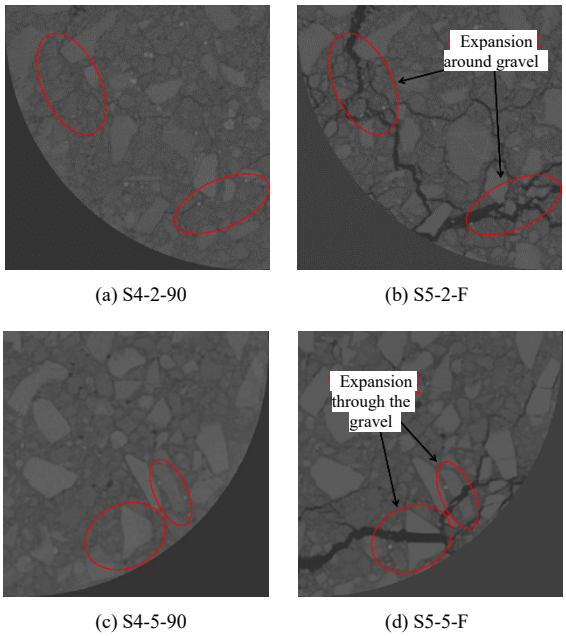

(a) S4-2-90 (b) S5-2-F

(c) S4-5-90 (d) S5-5-F

Fig. 9 1/4 selections of 2D fracture slice diagram of grouted specimen

The fracture development path is mostly caused by the damage of cement-based materials between large-size gravels. One is that the strength of large-size gravels is higher than that of cement-based materials. The second is the existence of the water film layer on the surface of gravels, resulting in a higher water−cement ratio near the gravel and the structure is loose within the interface transition zone, which becomes the weak part of the specimen. In this fashion, the development of fractures is mostly along the gravel boundaries and towards the direction of the maximum principal stress.

As shown in Fig.9, the intra-gravel fracture (fracture develop through the gravel body) is almost perpendicular to the gravel surface, and the fracture width is obviously larger than that of inter-gravel fracture (fracture develops along the gravel boundaries). When the fracture propagating encounters gravel, some of the fractures perpendicular to the gravel gradually become thicker to accumulate energy for subsequent propagation. According to the theory of stress intensity factor in fracture mechanics[26], the fracture shape Y, fracture size L, and far-field stress σ_a will affect the stress field strength at the fracture tip. When the strength factor K at the fracture tip reaches the fracture toughness K_C of the gravel, the fractures continue to propagate through the gravel and release energy in the form of fracture energy. The fracture criterion can be calculated as[26]

$$K(Y,L,\sigma_a)=K_C \tag{2}$$

3.2 Analysis of 3D fracture structure characteristics

From the CT slices at different loading stages for the grouted specimen, 2D fracture propagation analysis is conducted to approximately understand the local fracture dynamic evolution process under the uniaxial loading stage. To obtain a detailed fracture distribution morphology and propagation process of the grouted specimen, based on the CT slice reconstruction, the reconstruction optimization process is performed using VG Studio MAX software. 3D fracture reconstruction images are obtained for the specimen under different loading levels, as seen in Fig.10.

Under compressive loading, the fracture volume and surface area of the grouted specimen at different loading stages can represent the extent of fracture occupancy and internal extension relative to space, in this way, the two indicators can be used to indicate the internal fracture development and overall damage extent of the test specimen. The fractures in the CT images are extracted and calculated to obtain the characteristic parameters of the fracture structure at different stages, as shown in Table 4.

Figs.11 and 12 show the variation trends of the number and volume of fractures in the whole life cycle of the test specimens. According to the size of fracture volume, the internal fracture volume and number of grouted specimens are classified into 6 categories, Figs.13 and 14 present the stacking histograms of fracture volume and number percentage.

Before the specimens are loaded, it is observed that there are 7 439 internal fractures with a total volume of 1 155.63 mm^3, and the number of fractures with 0.01 mm^3≤ V<0.05 mm^3 accounts for 52% of the total fractures, where V is the fracture volume. Based on the variation trend and proportion of structural characteristic parameters in each loading stage, the whole fracture development process of grouted specimens is divided into 4 stages according to the CT scan times under uniaxial compression:

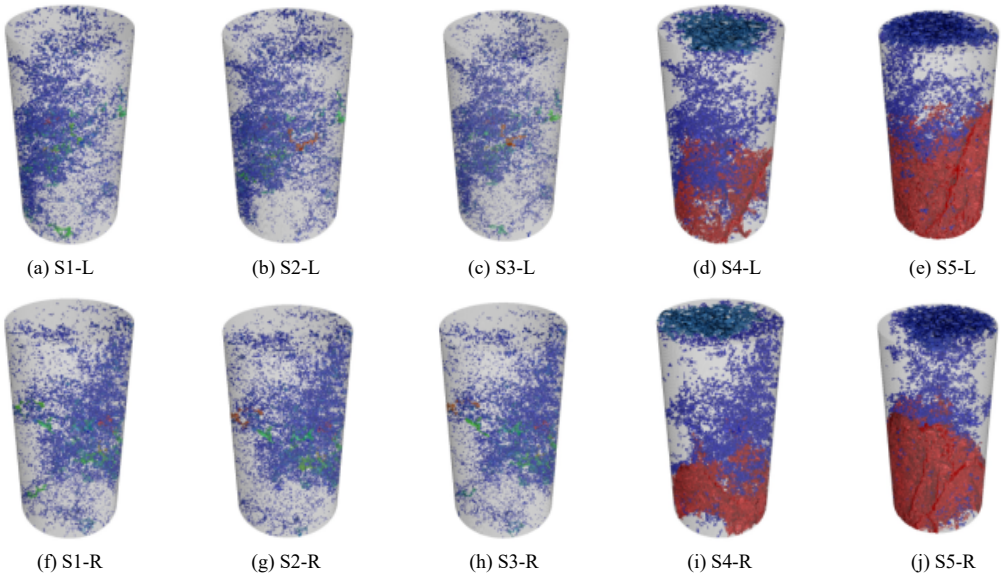

(a) S1-L (b) S2-L (c) S3-L (d) S4-L (e) S5-L

(f) S1-R (g) S2-R (h) S3-R (i) S4-R (j) S5-R

Note: The code rule in Fig.10 is: scan time-view angle, for example, S1-L and S1-R indicate the left front view and right front view of the first scan of the grouted specimen, respectively. The crack color in the reconstructed image is displayed according to the volume size, the red area indicates a large volume fracture, and the blue area indicates a small volume fracture.

Fig. 10 3D fracture reconstruction of grouted specimen

Initial defect propagation stage ($0<\sigma\leqslant 0.2\sigma_{max}$): In the 2nd scan, the porosity increases from 0.59% to 0.63%, the fracture number and volume increase by about 7%, and the fracture surface area increases by 5.5%. Among them, the fractures with 0.01 mm$^3\leqslant V<$0.05 mm^3 have the largest number of an increased degree. For the fractures with $V\geqslant$1 mm^3, the proportion of total fracture volume increases by 2%, the fracture number increases by 6.5%, however, the proportion decreases by 1%. It is observed that the connection of partial fracture occurs at this stage. Due to a large number of initial defects and poor stability inside the specimen, although there is a certain number of internal fracture volume compaction, more small volume fractures appear when the specimen is under a low stress level, resulting an overall increase of fracture volume and number at this stage.

Table 4 Characteristic parameters of fracture structure of grouting-reinforced body in different stages

CT scan times	Fracture number N	Fracture volume V/mm^3	Fracture area S/mm^2	Porosity P/%
1	7 439	1 155.63	21 676.35	0.59
2	8 011	1 243.90	22 879.14	0.63
3	7 369	1 161.53	21 586.88	0.59
4	2 701	3 145.59	58 887.73	1.60
5	2 504	12 000.39	162 906.33	6.11

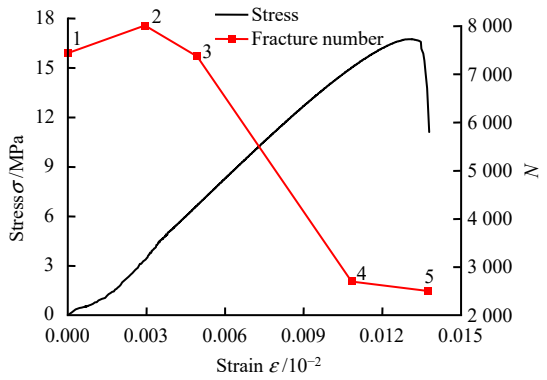

Fig. 11 Curves of fracture number and stress−strain

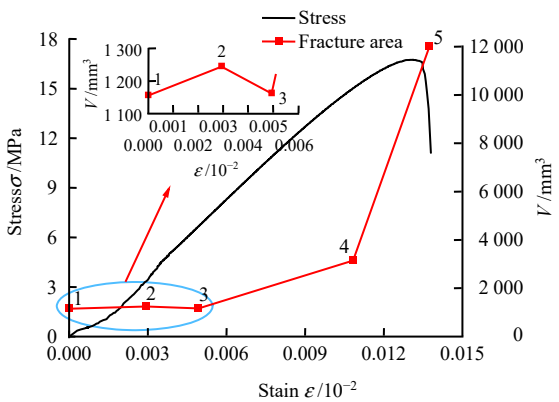

Fig. 12 Curves of fracture volume and stress−strain

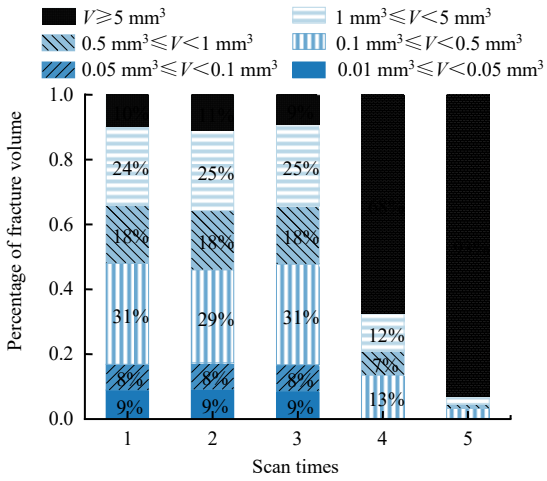

Fig. 13 Stacked histogram of fracture volume percentage

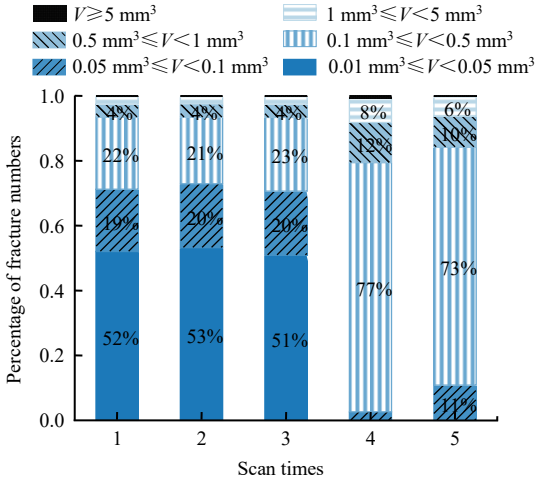

Fig. 14 Stacked histogram of fracture number percentage

Fracture compaction stage ($0.2\sigma_{max}<\sigma\leqslant 0.4\sigma_{max}$): In the 3rd scan, the fracture volume and number decrease by 6.62% and 8.01%, respectively. The porosity decreases to 0.59%, and the proportion of total fracture volume with $V\geqslant$1 mm^3 decreases by 2%. With the load increases, the friction force generated by the contact between the specimen end face and the metal indenter limits the lateral deformation. In the meantime, the end effect also affects the stress state near the end face of the specimen. A conical compression zone is formed under triaxial compression at both ends of the specimen. Part of the internal fracture within the zone is compressed and closed, resulting in a decreasing trend of the overall fracture characteristic parameters. Thus, as a whole, the compression part of the fractures inside the specimen is larger than the extended part, showing a slight decrease in the number, volume, and surface area of the fractures.

Fracture accelerated propagation stage ($0.4\sigma_{max}<\sigma\leqslant 0.9\sigma_{max}$): In the 4th scan, the total volume of fractures inside the specimen reaches 3 145.59 mm^3 with an increase of 170.81%. The fracture number decreases to 2 701 with

a decrease of 63.3%, and the porosity increases to 1.6%. Overall, the number of fractures with $V < 0.05$ mm^3 gradually decreases to 0, and the number and volume of fractures with $V \geqslant 0.1$ mm^3 show an increasing trend, among which the total volume and number of fractures with $V \geqslant 5$ mm^3 increase from 107.73 mm^3 to 2 124.24 mm^3 and from 14 to 17, respectively. At this stage, as the accelerated fractures evolve and the internal damage accumulates, the inclined fractures with large volumes appear at the lower part of the specimens (see Fig. 10(d)), which initially shows a penetration trend. The portion of the fracture propagation is much larger than the fracture compression. In this way, the fracture volume increases significantly, and the fracture numbers decrease significantly on the whole.

Fracture coalescence stage ($\sigma > 0.9\sigma_{max}$): In the 5th scan, the growth rate of fracture volume inside the specimen reaches the maximum value during the whole process, reaching 281.5% with a total volume of 12 000.39 mm^3. The porosity increases to 6.11%, the fracture number decreases by 7.29%, and the increasing extent of fracture surface area is 172.8%, which is similar to that of the 4th scan. The increasing load can cause rapid fracture coalescence inside the specimen. The volume of fractures with $V \geqslant 5$ mm^3 increases to 11 184.24 mm^3, accounting for 93% of the total fracture volume and the fracture number reduces to 8. After the stress on the specimen reaches the peak value, the fracture almost penetrates the whole specimen with a sharp stress decrease. The main fracture of macroscopic failure is formed on the surface, which propagates obliquely along the diagonal line. The internal fractures are distributed randomly and a complex fracture network structure is then formed in 3D space. The total volume reaches the maximum value of the whole life cycle, and finally, the specimen is sheared along the oblique section.

It is found that the specimen's internal fracture volume shows a trend of slow rise, slow decrease, slow rise, and rapid rise, and the fracture number shows a trend of increasing firstly and then decreasing during the whole compression stage. Different from the rock and concrete-like materials[17, 27], there is an initial defect propagation stage before the specimen enters the compacting stage. Because the indoor grouting mold is closed and the grouting pressure is small, part of the air in the mold cannot be discharged during grouting, resulting in a large volume and number of initial fractures within the specimen. Since the existence of many small volume defects, the instability of grouted specimen increases and the initial fractures develop more, leading to an increase in the volume and number of fractures at the early stage of loading. Subsequently, the internal fractures are compressed and closed when the specimens enter the compacting stage, and the overall fracture volume and number decrease. When the stress on the specimen is greater than the elastic limit stress, the specimen enters the fracture accelerated propagation stage, and the internal fractures propagate rapidly and coalescence, at this moment, the reduction extent of the fracture number is at the maximum value of the whole process. In the fracture coalescence stage, the internal fracture network structure is basically formed, and the phenomena of the fracture connection is reduced with a slight decrease in the fracture number. Due to the stress reaching the peak stress, the main fracture volume increases rapidly and the fracture volume increase is at the maximum value of the whole test process.

3.3 Damage evolution analysis

The failure process of concrete-like brittle materials such as grouting-reinforced bodies can be described as the following process: the internal micro-fracture continues to develop and evolve into macro-fracture, and eventually fail. A proper damage variable can establish a bridge that connects the macroscopic mechanical behavior of the material and the mesoscale damage law. From the principle of CT scanning, it is known that the specimen density is proportional to the gray value of the test result storage image, in this way, the CT number (the average gray value of the slice) can quantitatively describe the specimen density and the damage variation of the test specimen to a certain extent.

In this study, the 200th, 500th, and 700th layer images obtained by each scan are selected as representatives for calculation. The images are 8-bit stored gray images with the gray variation range of 0 to 255. Under the precondition of ensuring the same brightness and contrast of the selected images, the gray values of each slice are calculated using Python programming under the different stages and the results are given in Table 5. It can be seen that the average gray values of the initial slices are slightly different for the grouted specimens, which indicates a spatial non-uniformity of the initial fracture and material distribution inside the specimen.

Table 5 Average gray values of each slice under different load levels

Slice layers	Average gray values under different scan times				
	1 time	2 times	3 times	4 times	5 times
200th layer	113.42	112.85	113.76	105.16	87.73
500th layer	114.03	113.25	114.14	108.29	96.81
700th layer	113.73	113.10	113.98	109.25	103.64

For the calculation of damage variable D, in this study, a damage variable evolution equation derived by Ge et al.[28] is selected based on CT number:

$$D=\frac{\alpha_{\mathrm{f}}}{m_0^2}\left(1-\frac{1\,000+H_{\mathrm{i}}}{1\,000+\alpha_{\mathrm{f}}H_0}\right) \tag{3}$$

where α_{f} is the initial damage factor; m_0 is the density resolution of the CT device; H_{i} and H_0 are the CT number of damaged and undamaged in the selected area, respectively.

The evolution trend of the damage variable is calculated and plotted by substituting the gray value results of Table 5 into Eq.(3), as shown in Fig.15. It can be observed that when the stress is $\sigma<0.4\sigma_{\max}$, the increase or decrease of damage variable is not notable, indicating that there is a slight change of fractures in the space and volume inside the specimen, but the overall mechanical properties of the specimen remain basically unchanged. In addition, when $0.4\sigma_{\max}\leqslant\sigma<0.9\sigma_{\max}$, the damage variable increases rapidly, and the internal fracture of the specimen enters the unstable propagation stage. At this stage, the fracture develops rapidly and the overall damage is serious. Further, when the stress reaches the peak load, the internal fracture penetrates and propagates rapidly, and the slope of the damage variable evolution curve reaches the maximum value of the whole process. At this moment, the fracture evolves in the stage of the fastest evolution speed until the specimen is destroyed.

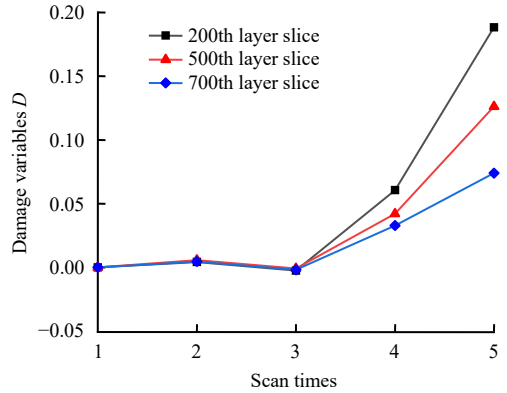

Fig. 15 Evolution trends of damage variables

Based on the fractal theory, the irregularity of CT slices and the complexity of fracture evolution are characterized. The mesoscale damage extent of the specimen is further analyzed at different stages. The fractal dimension of the gray image of slice $M\times M$ (M is the image pixel) is calculated as follows:

$$D_{\mathrm{f}}=\lim_{r\to 0}\frac{\ln N_{\mathrm{r}}}{\ln(1/r)} \tag{4}$$

where $N_{\mathrm{r}}=\sum_{i,j}n_{\mathrm{r}}(i,j)$; N_{r} and n_{r} are the number of boxes covering all grids and the (i, j)th grid, respectively; $r=k/M$; k is the division precision. By varying the value of precision k, linear regression is conducted on the calculated $\ln(1/r)$−$\ln N_{\mathrm{r}}$, and the slope of the final fitting curve is the fractal dimension D_{f}.

Figure16 shows the calculation results of the fractal dimension for each stage of the specimen 200th layer, and the R^2 is above 0.975, meaning a high accuracy calculation. For the same layer of CT slices, the larger the black area representing the fracture area, the larger the fractal dimension calculated by Eq.(3). The evolution trend of fractal dimension for different slice layers is plotted, as seen in Fig.17. It is seen that for each layer slice, the evolution of fractal dimension and damage variable have a similar trend in the loading process, that is slow rise, slow decrease, slow rise, and rapid rise. When the specimen stress is $\sigma<0.4\sigma_{\max}$, the speed of internal fracture evolution is slow, the slice is not complicated and the fractal dimension basically remains the same. When $\sigma\geqslant0.4\sigma_{\max}$, the specimen internal fracture gradually propagates and penetrates. The slice becomes even more complicated and the fractal dimension accelerates rapidly. The fractal dimension reaches the maximum value of the whole process when the specimen enters the residual stress stage after the peak load.

4 Conclusion

Based on the digital image processing method, the CT images of the grouted specimen are reconstructed under uniaxial compressive loading, and the dynamic evolution of the internal fracture is reflected visually. The characteristic parameters of the specimen and the gray values of the slices are then extracted and calculated. The fractal dimension of the slices is also calculated using the differential dimension method. The main conclusions are as follows:

(1) In terms of the quantitative characterization and analysis of the slice fracture area, it is found that the grouted specimen fractures propagate along the boundaries under the uniaxial load. When the fracture propagation encounters gravel, most of the fractures propagate around the gravel boundaries and few fractures propagate through the gravel. In addition, the fracture bifurcation propagation mostly occurs at the interface between the cement matrix and gravel.

(2) The internal fracture volume of the grouted specimen shows an overall trend of a slow rise−slow decrease−slow rise−rapid rise, which corresponds to the four stages of the failure process: initial defect propagation stage−fracture compaction stage−fracture accelerated propagation stage−fracture coalescence stage. The fracture connection

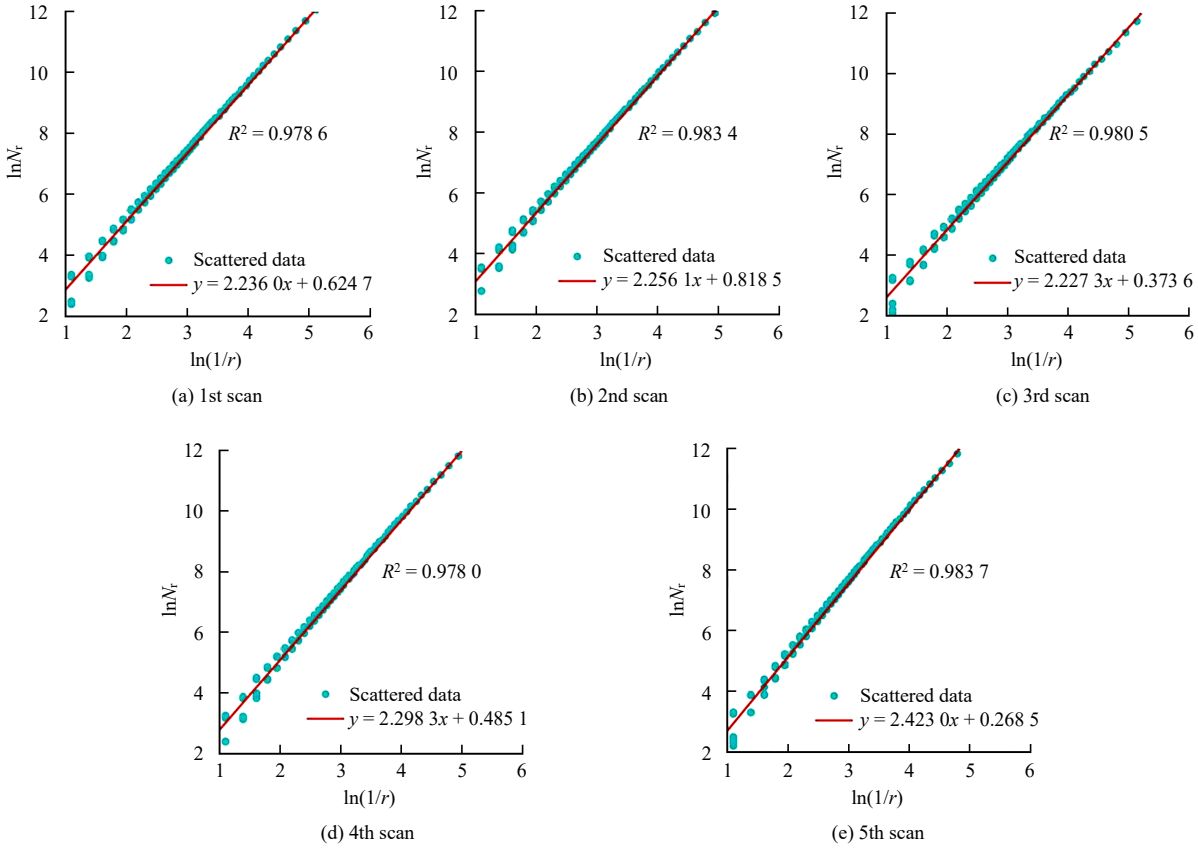

Fig. 16 Calculation results of fractal dimension of 200th slice

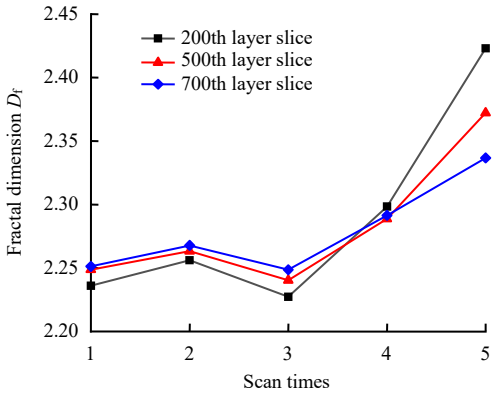

Fig. 17 Evolution trend of fractal dimension

phenomenon mainly occurs in the fracture accelerated propagation stage. At this stage, the decreasing of fracture number is at the maximum value of the whole testing process, which can reach up to 63.3%. The fracture propagation evolution mainly occurs in the fracture coalescence stage, at this time interval, the increasing of fracture volume is at the maximum value of the whole testing process, reaching 285.1%. In addition, when the grouted specimen is in the failure state, the internal fractures mostly associate with relatively large volume fractures with $V \geqslant 5$ mm^3, which accounts for 93% of the total fracture volume.

(3) The variation of damage variables D and fractal dimension D_f can be good indicators to reflect the fracture evolution law of the grouted specimen under loading condition. For the slice at the same loading stage of the test specimen, it is found that the values of damage variable and fractal dimension have a certain positive correlation, and it is similar to the evolution trend of fracture volume, which indirectly reflect the damage variation characteristics for the loading specimen due to the fracture development.

References

[1] CHEN Xiang-sheng, FU Yan-bin, CHEN Xi, et al. Progress in underground space construction technology and technical challenges of digital intelligence[J]. China Journal of Highway and Transport, 2022, 35(1): 1−12.

[2] VON DER TANN L, STERLING R, ZHOU Y X, et al. Systems approaches to urban underground space planning and management - a review[J]. Underground Space, 2020, 5(2): 144−166.

[3] SHA Fei, LI Shu-cai, LIN Jin-chun, et al. Research on penetration grouting diffusion experiment and reinforcement mechanism for sandy soil porous media[J]. Rock and Soil Mechanics, 2019, 40(11): 4259−4269.

[4] LI Shu-cai, FENG Xiao, LIU Ren-tai, et al. Study on infiltration

coefficient and reinforcing mechanism of grout suspension in sandy soil medium[J]. Chinese Journal of Rock Mechanics and Engineering, 2017, 36(Suppl.2): 4220−4228.

[5] ZHU Jiang, LI Guo-zhong. Performance of thermal insulation materials of polypropylene fiber reinforced vitrified small ball[J]. Journal of Building Materials, 2015, 18(4): 658−662, 703.

[6] WANG Zhi-hang, XU Jin-yu, LIU Gao-jie, et al. Effect of UV aging on shear properties and pore structure of polymer-based composites[J]. Materials Reports, 2022, 36(2): 214−219.

[7] ZHOU Ming-ru, PENG Xin-xin, SU Bo-tao, et al. Grouting performance of ordinary cement and superfine cement and comparison of grouting effect in loess[J]. Bulletin of the Chinese Ceramic Society, 2017, 36(5): 1673−1678.

[8] WANG Zhi, LI Long, WANG Zhao-ya. Experimental study on failure of cracked rock-like material after grouting reinforcement[J]. Journal of Central South University (Science and Technology), 2018, 49(4): 957−963.

[9] WANG Hai-long, RONG Mi-ren, DONG Hao, et al. Influence of strain rate on mechanical properties of grouting body[J]. Journal of Harbin Institute of Technology, 2020, 52(9): 176−184, 192.

[10] WANG Zhi, QIN Wen-jing, ZHANG Li-juan. Experimental study on static and dynamic mechanical properties of cracked rock after grouting reinforcement[J]. Chinese Journal of Rock Mechanics and Engineering, 2020, 39(12): 2451−2459.

[11] WANG Qi, WANG Lei, LIU Bo-hong, et al. Study of void characteristics and mechanical properties of fractured surrounding rock grout[J]. Journal of China University of Mining & Technology, 2019, 48(6): 1197−1205.

[12] LE H L, SUN S R, KULATILAKE P, et al. Effect of grout on mechanical properties and cracking behavior of rock-like specimens containing a single flaw under uniaxial compression[J]. International Journal of Geomechanics, 2018, 18(10): 4018129.

[13] LU Hai-feng, CAO Ai-de, LIU Quan-sheng, et al. Experimental study on mechanical properties of grouting consolidating bodies with inner defects[J]. Chinese Journal of Rock Mechanics and Engineering, 2020, 39(8): 1560−1571.

[14] LIU Y T, CHEN B. Research on the preparation and properties of a novel grouting material based on magnesium phosphate cement[J]. Construction and Building Materials, 2019, 214: 516−526.

[15] LI Shao-feng, LI Shu-cai, LIU Ren-tai, et al. Development of the grouting material for reinforcing water-rich broken rock masses and its application[J]. Rock and Soil Mechanics, 2016, 37(7): 1937−1946.

[16] ZHANG Guo-kai, LI Hai-bo, XIA Xiang, et al. Effects of microstructure and micro parameters on macro mechanical properties and failure of rock[J]. Chinese Journal of Rock Mechanics and Engineering, 2016, 35(7): 1341−1352.

[17] ZHANG Yan-bo, XU Yue-dong, LIU Xiang-xin, et al. Quantitative characterization and mesoscopic study of propagation and evolution of three-dimensional rock fractures based on CT[J]. Rock and Soil Mechanics, 2021, 42(10): 2659−2671.

[18] YANG Ren-shu, XUE Hua-qun, GUO Dong-ming, et al. Laboratory grouting experiment based CT analysis of grouted soft rocks in deep mines[J]. Journal of China Coal Society, 2016, 41(2): 345−351.

[19] BHARATH G, SHUKLA M, NAGABUSHANA M N, et al. Laboratory and field evaluation of cement grouted bituminous mixes[J]. Road Materials and Pavement Design, 2020, 21(6): 1694−1712.

[20] ZHU Lin, DANG Fa-ning, DING Wei-hua, et al. Coupled X-ray computed tomography and grey level co-occurrence matrices theory as a method for detecting microscopic damage of concrete under different loads[J]. China Civil Engineering Journal, 2020, 53(8): 97−107.

[21] FAN Z Y, SUN Y M. A study on fatigue behaviors of concrete under uniaxial compression: testing, analysis, and simulation[J]. Journal of Testing and Evaluation, 2021, 49(1): 160−175.

[22] SUN Hao-kai, GAO Yang, ZHENG Xin-yu, et al. Failure mechanism of precast defective concrete based on image statistics[J]. Journal of Building Materials, 2021, 24(6): 1154−1162.

[23] LIU Xiang-yang, CHENG Ye, LI Ming-jing, et al. Theoretical research on longitudinal fracture grouting of deep buried strata based on slurry rheology[J]. Rock and Soil Mechanics, 2021, 42(5): 1373−1380.

[24] AVCI E, MOLLAMAHMUTOGLU M. Strength and permeability characteristics of superfine cement and fine fly ash mixture grouted sand[J]. ACI Materials Journal, 2020, 117(6): 293−304.

[25] HWANG C L, HSIEH S L. The effect of fly ash/slag on the property of reactive powder mortar designed by using Fuller's ideal curve and error function[J]. Computers and Concrete, 2007, 4(6): 425−436.

[26] XIE He-ping, PENG Rui-dong, ZHOU Hong-wei, et al. Research progress of rock strength theory based on fracture mechanics and damage mechanics[J]. Progress in Natural Science, 2004, 14(10): 7−13.

[27] WANG Deng-ke, ZHANG Hang, WEI Jian-ping, et al. Dynamic evolution characteristics of fractures in gas-bearing coal under the influence of gas pressure using industrial CT scanning technology[J]. Journal of China Coal Society, 2021, 46(11): 3550−3564.

[28] GE Xiu-run, REN Jian-xi, PU Yi-lin. Macro-meso experimental study on geotechnical damage mechanics[M]. Beijing: Science Press, 2004: 138−143.